Journal of Materials Chemistry B

ROYAL SOCIETY OF CHEMISTRY

PAPER

View Article Online
View Journal | View Issue

Cite this: J. Mater. Chem. B, 2023, 11, 3097

Revealing drug release and diffusion behavior in skin interstitial fluid by surface-enhanced Raman scattering microneedles†

Shang Shi,[ab] Yunqing Wang,*[a] Rongchao Mei,[a] Xizhen Zhao,[a] Xifang Liu[c] and Lingxin Chen *[ad]

Microneedle (MNs), as a novel dermal drug delivery formulation, have drawn a lot of attention in recent years. Drug release and diffusion behavior in dermal interstitial fluid (ISF) determines the pharmacokinetics and effectiveness of MNs, which have not been clearly elucidated until now. Herein, we develop surface-enhanced Raman scattering (SERS)-based detection MNs (D-MNs) for the sensitive analysis of model drugs in ISF. The surface of the D-MNs was deposited with a high density of hotspot-rich core–satellite gold nanoparticles, which would generate a sensitive SERS signal of a model drug (3,3′-diethylthiatricarbocyanine, DTTC) released by therapeutic MNs (T-MNs). Furthermore, the D-MNs produced an internal-standard signal for drug signal calibration, increasing the accuracy of detection. Taking advantage of the D-MNs, the release and diffusion behavior of the drug from T-MNs in the ISF of living mice was systematically studied. It was found that DTTC diffused without directional preference in ISF up to a distance of 1.5 cm. The intensities at diffusion sites decreased sharply with increasing distance from the release site (less than 0.3% at 1.5 cm). These results indicated that drug concentration gradient rather than ISF fluidity was a major driving force for the diffusion. Moreover, the application of water-soluble MN polymers, hydrophilic model drugs in T-MNs, as well as a heating or cupping treatment of mouse skin, enhanced drug diffusion in ISF. This work provides a new tool for *in situ* and real-time detection of molecules in ISF, which would be beneficial for the development and evaluation of MN-based therapeutic systems.

Received 29th November 2022,
Accepted 9th March 2023

DOI: 10.1039/d2tb02600g

rsc.li/materials-b

Introduction

Microneedles (MNs) are a novel transdermal drug delivery system, which typically load therapeutic drugs within an array of polymeric needles with a length of 10–2000 μm.[1] They can penetrate the stratum corneum and create microporous channels to release drugs into the dermal interstitial fluid (ISF) without damaging nerves or capillaries, and have attracted increasing attention for their painless, easy self-administration, and prominent therapeutic effects.[2,3] MNs have become an emerging technology in cutting-edge biomedical fields, especially in therapy[4–6] and biomarker detection.[7–9]

Dermal ISF is the first biological reservoir after the puncture of MNs into the skin.[10–12] ISF is a fluid that flows between the blood and lymphatic vessels through the extracellular matrix of tissues.[13] With swelling or dissolution of the polymer substrate of MNs, the loaded drugs are released to ISF and undergo both vertical and lateral diffusion in this fluid.[14,15] Vertical diffusion is driven mainly by the concentration gradient of the drug, which makes the drug molecules cross the ISF layer, reach the deeper blood capillary, and transfer to the whole body *via* blood circulation. The vertical diffusion rate determines the onset and duration times of an MN formulation. Simultaneously, lateral diffusion of the drugs also occurs, which is dominated not only by concentration gradient-driven molecular diffusion but also the potential flow property of ISF. Lateral diffusion influences the spread area of the released drugs in dermal tissue, which is an indicator for evaluating drug absorption. The drug release and diffusion processes play a crucial role in the regulation of MN effectiveness and would be influenced by various aspects not only from the MNs (such as delivery polymer or drugs) but also from the ISF (such as flow rate or osmotic pressure). To date, detailed information has not been fully understood owing to the lack of ideal analytical methods.

Dermal ISF analysis faces the following difficulties. One is the accuracy of the sampling or analysis site in the skin of living

[a] CAS Key Laboratory of Coastal Environmental Processes and Ecological Remediation, Yantai Institute of Coastal Zone Research, Chinese Academy of Sciences, Yantai, 264003, China. E-mail: yqwang@yic.ac.cn, lxchen@yic.ac.cn
[b] University of Chinese Academy of Sciences, Beijing, 100049, China
[c] Linyi Central Blood Station, Linyi, 276000, China
[d] School of Pharmacy, Binzhou Medical University, Yantai, 264003, China

† Electronic supplementary information (ESI) available. See DOI: https://doi.org/10.1039/d2tb02600g

animals. Dermal ISF merely locates at a depth of 0.2–2 mm, and it is challenging to detect drugs in ISF by applying traditional analytical protocols to the transdermal drug delivery system.[16] For example, the Franz diffusion cell approach[17] is an *in vitro* method which can only provide drug penetration information across *ex vivo* skin. Tape stripping[18] is used to obtain the stratum corneum after exposing the skin to drugs, and then analyzing the content of substances in the tape. Microdialysis[19] enables ISF analysis, relying on passive drug diffusion from ISF to the buffer solution in an implantable probe, but the protocol is complicated (requiring an external pump to supply the fluid), time-consuming, and cannot achieve a real-time readout of results. Apart from sampling site accuracy, another difficulty is the low volume of ISF (*i.e.*, the low amount of drug) that can be extracted for analysis, which requires high sensitivity from analytical techniques. In the context of the successful development of MN formulations, there is an urgent need to develop analytical techniques for the *in vivo*, real-time monitoring of drugs in ISF, which will be beneficial for (1) gaining fundamental knowledge about ISF properties, (2) screening new drug delivery materials and preparation protocols for controlled-released MNs, and (3) point-of-care monitoring of the safe application of MNs loaded with narrow therapeutic window concentrations.[20–22]

Herein, we propose a proof-of-concept method to investigate drug release and diffusion in ISF by combining site-directed MN technology and the ultrasensitive surface-enhanced Raman scattering (SERS) method. MN technology has been adapted for ISF collection[23] and biomarker detection[24] in ISF, which ensures the sensing site well matches the drug release depth of MN formulations. SERS is an ultrasensitive vibrational spectroscopy technique showing great potential for *in vivo* detection.[25] A SERS-based MN sensing platform has proved to be a promising tool for the *in situ* fast detection of biological species in ISF such as glucose,[26] H^+,[27] and bacterial metabolites,[28] which was improved for drug diffusion monitoring in this work. The experimental design is demonstrated in Fig. 1. Two types of MN, *i.e.*, a therapeutic MN (T-MN) and a SERS detection MN (D-MN) were involved in the experiment. The T-MN was made of hyaluronic acid as the drug-loading material and 3,3′-diethylthiatricarbocyanine (DTTC) as the model drug. Because the two MNs have the same length, DTTC drug molecules from T-MN diffused to ISF could be adsorbed by the D-MN at a given distance away and the SERS signal can be detected *in situ*.

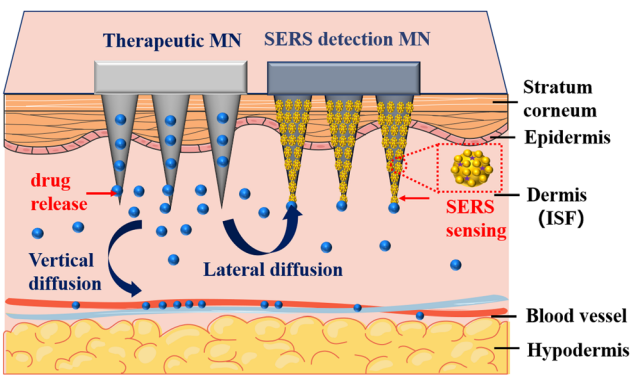

Fig. 1 Scheme of the study of drug release and diffusion behavior of a therapeutic microneedle (T-MN) *via* a SERS detection microneedle (D-MN) in dermal interstitial fluid (ISF).

Results and discussion

Preparation and characterization of T-MN and D-MN

Therapeutic microneedles (T-MNs) were synthesized with hyaluronic acid (HA) polymer, which is a glycosaminoglycan that is an intrinsic component of connective tissue and dermis.[29] Its excellent solubility and biocompatibility make it an ideal carrier for the delivery of rapid-release drugs.[30,31] DTTC was selected as a model drug. It is a photosensitizer for photodynamic treatment[32] with an excellent SERS signal, giving it a satisfactory detection limit for detection. T-MNs were prepared in a PDMS mold and neatly arranged in a 10 × 10 array (Fig. 2a). A blue color indicated DTTC was successfully loaded into the MNs. An SEM image showed that the tips were uniform and the height was around 800 μm (Fig. 2b). They demonstrated excellent mechanical strength that could penetrate the skin of a living mouse (Fig. S1a, ESI†). H&E results showed that the puncture depth is about 200 μm, which is sufficient to deliver the drug into the ISF (Fig. S1b, ESI†). 10 min after the removal of the T-MNs, the microholes in the skin disappeared, suggesting the biosafety of the MNs (Fig. S2a, ESI†).

Detection microneedles (D-MNs) were prepared with polymethyl methacrylate (PMMA) polymer, which had high mechanical strength for skin penetration and high light transmission for SERS signal collection. Core–satellite gold nanoparticles (AuNPs) were deposited on the PMMA tips to achieve SERS sensing capability *via* three steps: (1) spherical core AuNPs were synthesized and adsorbed on PMMA MNs by using polystyrene-*block*-poly(4-vinylpyridine) (PS-*b*-P4VP) copolymer as "glue"; (2) 4-mercapto benzonitrile (4-MBN) Raman reporter was bonded to core AuNPs through Au–S bonds, producing an internal standard (IS) signal; (3) satellite AuNPs were grown *in situ* on each core, forming core–satellite AuNPs on PMMA MNs. The rough surfaces of the resultant NPs are rich in hotspots, endowing them with high adsorption capacity and strong SERS detection ability. Moreover, the embedded alkynyl-containing 4-MBN between the core and satellite AuNPs generates distinguishable SERS signals in the "Raman silent" region as an IS, which can greatly eliminate detection errors.

The D-MNs showed neatly arranged 3 × 3 arrays of tips on a 0.5 × 0.5 cm array that were approximately 800 μm and conical in shape (Fig. 2c), and also showed ideal mechanical strength for skin penetration (Fig. S1c and S2b, ESI†). H&E results showed a puncture depth of 200 μm, which is consistent with the T-MNs (Fig. S1d, ESI†). In addition, SEM images showed that core–satellite NPs were uniformly distributed on the MN surface with a size of about 70 nm and a density of about 114 NPs per μm^2 (Fig. 2d). The SERS signal detection performance was investigated with DTTC-loaded gel serving as an *in vitro* simulant of ISF (Fig. 2e and Fig. S4, ESI†). The 2220 cm^{-1} peak of blank D-MNs (IS signal) was located in the "Raman silent" region,

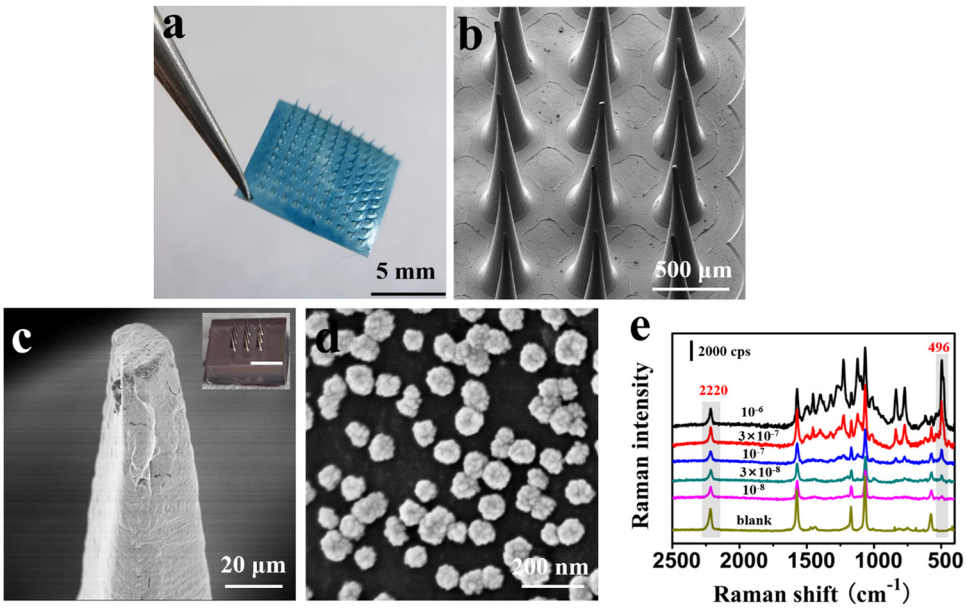

Fig. 2 Characterization of T-MNs and D-MNs. (a) Image of DTTC-loaded T-MNs with a 10 × 10 array. (b) SEM images of the T-MNs. (c) SEM image of the tip of a D-MN. The inset shows a photograph of a D-MN (scale bar: 0.25 cm). (d) High magnification SEM image of the D-MN tip, showing the high density of core–satellite AuNPs. (e) SERS spectra of DTTC detected by D-MNs incubated in agarose gel loaded with different concentrations of DTTC. The peak of DTTC at 496 cm^{-1} can be distinguished from the IS peak of D-MNs (2220 cm^{-1}).

which could clearly be distinguished from the characteristic peak of DTTC at 496 cm^{-1}. The D-MNs demonstrated satisfactory sensitivity towards DTTC, which could be detected at a concentration as low as 10^{-8} M. Without IS calibration, the RSD of DTTC intensities (I_{496}) was 32%. By contrast, after introducing the IS signal, the RSD of the intensity ratios (I_{496}/I_{2220}) was significantly reduced to 9.68% (Fig. S3, ESI†). The calibration effect guaranteed accuracy and reproducibility for analyte detection. The curve of DTTC concentration and I_{496}/I_{2220} ratio was fitted for quantitative analysis (Fig. S4, ESI†). In addition, the loss of AuNPs from the D-MNs after skin puncture was evaluated *via* ICP-MS detection. The amount of gold element was only reduced by 5.6% per MN from 3.92 μg to 3.70 μg (Fig. S5, ESI†). The few lost AuNPs may not affect the biosafety of the MNs.

Drug release and diffusion behavior in ISF

ISF is a novel target for dermal drug administration, and drug diffusion behavior in ISF has not been clarified until now. Taking advantage of T-MNs and D-MNs, this issue was explored for the first time. As indicated in Fig. 3a, T-MNs were stuck into the skin of a living mouse for 10 min, which ensured the tips detached from the MNs with the dissolution of HA polymer in ISF for continuous DTTC release. Subsequently, the T-MNs were removed, followed by the sticking of D-MNs into both the release site (T-MN site) and diffusion sites with specific directions and distances from the release site. After 10 min incubation, the D-MNs were removed for SERS signal detection.

The lateral diffusion of DTTC was investigated first. The experimental design is shown in Fig. 3b and c. After removing the T-MNs, five D-MNs were quickly inserted into the skin. One was located at the release site (marked "0") and the other four were located around the "0" site (marked "a" to "d") at equal distances of 0.5 cm. After 10 min incubation, the characteristic peak of DTTC at 496 cm^{-1} was detected from all sites. The normalized DTTC intensity (I_{496}/I_{2200}) of the "0" site was 26.7, which was much higher than those of the diffusion sites, ranging from 0.62 to 1.14. These results implied that only 0.014 μM to 0.059 μM DTTC could be detected at the diffusion sites (according to the quantitative curve in Fig. S4, ESI†), and a majority of DTTC molecules were still at the release site after 10 min without fast lateral diffusion. Also, the diffusion was not in specific orientations, as indicated by the small ratio differences among the MNs in the four directions. Furthermore, diffusion distance was explored in a separate experiment by simultaneously placing four D-MNs along one direction with a gap of 0.5 cm (Fig. 3e). The results showed that DTTC can be detected as far as 1.5 cm, and the normalized SERS intensities decrease with the increase in distance, which were 2.57%, 1.07%, and 0.27% of that at "0" site intensity at distances of 0.5 cm, 1 cm, and 1.5 cm, respectively (Fig. 3d and e). Generally, drugs move through blood vessels, so the concentration of the drug in blood measured according to the change in location should not show a significant change. Our results indicated that this was not the case in ISF, where drugs were mostly adsorbed locally and lateral diffusion was slow. The main reason is that, although ISF is rich in water and soluble molecules, it is in a gel state and cannot flow as freely as blood. The drug diffusion is driven by concentration gradients and the weak fluidity of ISF. The diffusion of various solutes in ISF is hindered by the gel. Therefore, the Raman peaks at the injection site were much more intense than those from the diffusion sites centimeters away.

Then the concentration evolution of DTTC in ISF at two sites (0 and 0.5 cm) was studied. After the administration of T-MNs,

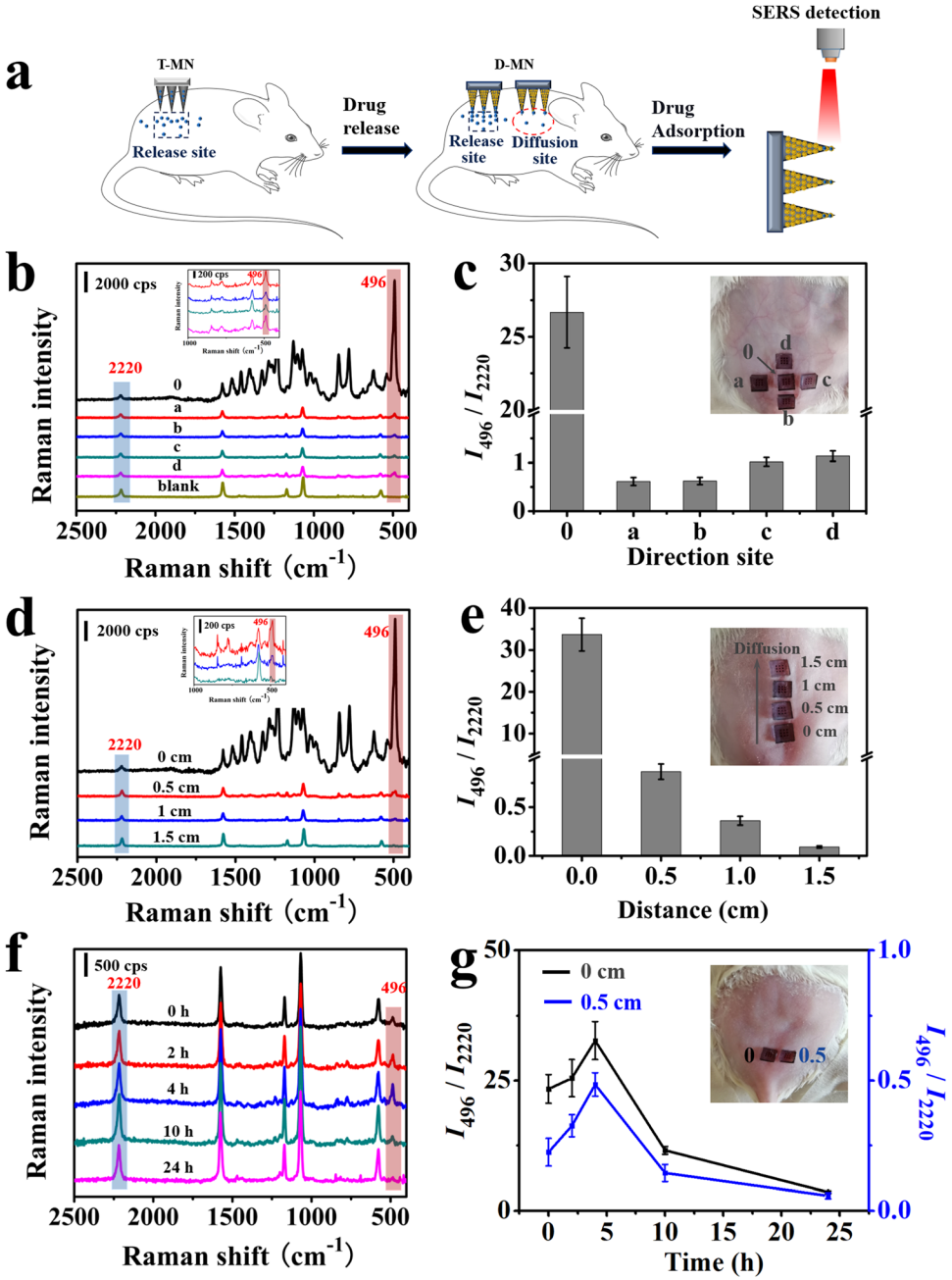

Fig. 3 (a) Flow chart of the investigation of diffusion behavior of DTTC in ISF *via* T-MNs and D-MNs. (b) SERS spectra of DTTC detected by D-MNs at the drug release site (0) and four diffusion sites (a to d). The inset shows enlarged DTTC spectra at 496 cm^{-1} at the four diffusion sites. (c) Histogram of SERS intensity ratio I_{496}/I_{2220} (n = 6). The inset shows the distribution of D-MNs on the mouse skin. (d) SERS spectra of DTTC detected by D-MNs at the drug release site (0 cm) and three diffusion sites (0.5 cm, 1 cm, 1.5 cm) in a line. The inset shows enlarged DTTC spectra at 496 cm^{-1} at the three diffusion sites. (e) Histogram of the SERS intensity ratio I_{496}/I_{2220} for different diffusion distances (n = 6). The inset shows the distribution of D-MNs on the mouse skin. (f) SERS spectra of DTTC at 0.5 cm site at different times. (g) Evolution of the SERS intensity ratio I_{496}/I_{2220} at the release and diffusion sites (n = 6).

SERS intensities at the two sites were monitored at 0, 1, 4, 10, and 24 h by using fresh D-MNs at each time point. The results showed that there was a similar concentration evolution trend between the two sites. The value of I_{496}/I_{2200} increased from 0 to 4 h and then decreased from 4 to 24 h (Fig. 3f, g and Fig. S6a, ESI†). The signal increase within 4 h could probably be attributed to the continuous release of DTTC from the high concentration of HA-DTTC mixture trapped in microholes. After this release process, the concentration sharply decreased at 10 h and was almost undetectable at both sites, mainly owing to the loss of DTTC from ISF to deeper tissues through vertical diffusion. Confocal fluorescence microscopy images captured from skin tissues at the drug release sites (after 4 h) verified this process (Fig. S6b, ESI†). Red fluorescence of DTTC could be observed diffusing from MN-induced microholes to the fat layer at 700 μm depth below the capillaries.

The above results demonstrated that: (1) DTTC diffused uniformly without direction preference in ISF, (2) the concentration was distance- and time-dependent, and (3) an overwhelming majority of DTTC was absorbed *in situ* at the release site, hinting that ISF was in a gel rather than a fluid state with fast flow speed.[33] The diffusive movement of molecules occurred within the gel and the major driving force was the concentration gradient.

Influencing factors for drug release and diffusion in ISF

Four factors potentially affecting drug release and diffusion in ISF were investigated, covering not only the features of MNs but also the skin condition of the mice. The solubility of carrier polymer plays an important role in regulating release rate from MNs, thus sodium alginate (SA)-based T-MNs were prepared for comparison with the above-mentioned HA-MNs (Fig. S7, ESI†). SA is a popular biocompatible natural polysaccharide for MN production. In the presence of Ca^{2+}, it cooperatively interacts with blocks of α-L-guluronic acid monomers to form ionic bridges and thus induce gelation of SA.[34] Unlike HA, SA polymer swells instead of dissolving in ISF and shows a sustainable rather than immediate drug release feature.[35] Our results verified the difference between the two polymers by the dramatic difference in the I_{496}/I_{2200} value (23.4 *vs.* 2.99) for HA and SA MNs (Fig. 4c). For HA MNs, the SERS intensity reached a maximum at 4 h, rapidly decreased during 4 to 24 h, and then the signal disappeared at 48 h. In contrast, SA MNs demonstrated a lagged profile. The I_{496}/I_{2200} value increased slowly and reached a maximum at 10 h. Moreover, the signal of SA MNs was more durable (Fig. 4b), being twice as long as that of HA MNs (96 h *vs.* 48 h).

The amphiphilicity of drugs affects the penetration and distribution in the skin and needs to be considered during MN design. Water-soluble crystal violet (CV)-loaded HA MNs were prepared to compare with lipophilic DTTC-loaded MNs (Fig. 4d). The results showed that the characteristic peak of CV (1610 cm^{-1}) could be detected in ISF (Fig. 4e). Unlike the "up-down" evolution curve of DTTC, the intensity of CV continuously decreased with an elapse of time. Additionally, the signal of CV completely disappears at 24 h (Fig. 4f), which was earlier than that of DTTC (48 h). These results indicated that CV diffused faster than DTTC in ISF. The reason might be that the majority of the components in ISF are hydrophilic HA,[36] resulting in faster diffusion or capillary absorption of hydrophilic CV rather than pre-accumulating in the ISF like a reservoir based on the principles of similarity and compatibility.

Clinically, skin heating is used to promote drug absorption by the skin and to increase the bioavailability of transdermal patches.[37] These heat-enhanced patches have been successfully applied to the dermal delivery of corticosteroids[38] and local anesthetics.[39] The effect of skin temperature on drug diffusion in ISF was investigated for the first time. After the removal of DTTC-loaded T-MNs, the mice were kept under room temperature conditions or heating lamp irradiation conditions, making the skin temperatures 26.5 °C and 40 °C, respectively (Fig. S8, ESI†). SERS detection was performed at the release site (0 site) at 0, 2 and 4 h (Fig. 4g). The results showed that the initial drug release measured at 0 h was nearly uniform, and the measured I_{496}/I_{2200} values continued to increase from 0 to 4 h at 26.5 °C, and increased from 0 to 2 h and decreased from 2 to 4 h at 40 °C (Fig. 4h and i). On the one hand, increased temperature causes a shift from the gel state to the flow state of the ISF, which accelerates the diffusion of molecules in the ISF. On the other hand, capillary diastole, blood flow, and osmotic pressure increase.[40] These factors may force DTTC to permeate from the interstitium into the vasculature, resulting in a difference in the signal at room temperature.

Cupping, as a traditional Chinese medicine (TCM) treatment,[41] is more commonly used in TCM clinics. Cupping can change the tissue morphology of local skin, which is manifested by an obvious thickening of the skin epidermis, loose cell arrangement, expansion of blood vessels, and aggregation of blood cells in the dermis. These factors may affect absorption and diffusion after MN administration. Recently, a painless and effective method of delivering DNA was developed by combining MN technology with skin aspiration treatment similar to traditional cupping.[42] Based on this, we designed an experiment to study the effect of skin suction on drug diffusion behavior in ISF. After DTTC release from T-MNs, the mouse skin was repeatedly aspirated 5 times, lasting for 3–5 seconds each time, and negative pressure was applied (Fig. S9, ESI†). SERS intensities were detected before and after aspiration at the "0" site and 0.5 cm diffusion site (Fig. 4j). The results showed that the signal value of I_{496}/I_{2200} at the "0" site decreased from 16.57 to 11.85 (*i.e.*, DTTC concentration from 69 μM to 17 μM) after aspiration, while the signal value of I_{496}/I_{2200} at the diffusion site increased from 1.48 to 3.16 (*i.e.*, DTTC concentration from 0.091 μM to 0.38 μM) (Fig. 4k, i, and Fig. S4, ESI†). This may be because aspiration treatment enlarges the skin pores, promotes the dilatation of subcutaneous capillaries, and enhances ISF mobility. In addition, aspiration leads to a pressure difference between the inside and outside of the skin, and DTTC within the ISF is squeezed and diffused under the pressure effect.

Conclusions

In conclusion, we have proposed a proof-of-concept method to investigate drug release and diffusion in ISF by combining site-directed MN technology and the ultrasensitive surface-enhanced Raman scattering (SERS) method. It was found that DTTC was absorbed mostly at the site of drug release, a little diffused uniformly and without specific orientations in the ISF, and the concentration was time–distance dependent and could diffuse up to 1.5 cm. The use of water-soluble polymers and drugs in MN formulation, as well as the heating and suction of skin, promote the release and diffusion behavior of the drug in the ISF. These findings lay the foundation for screening carrier materials and clinical treatment methods for MN formulations

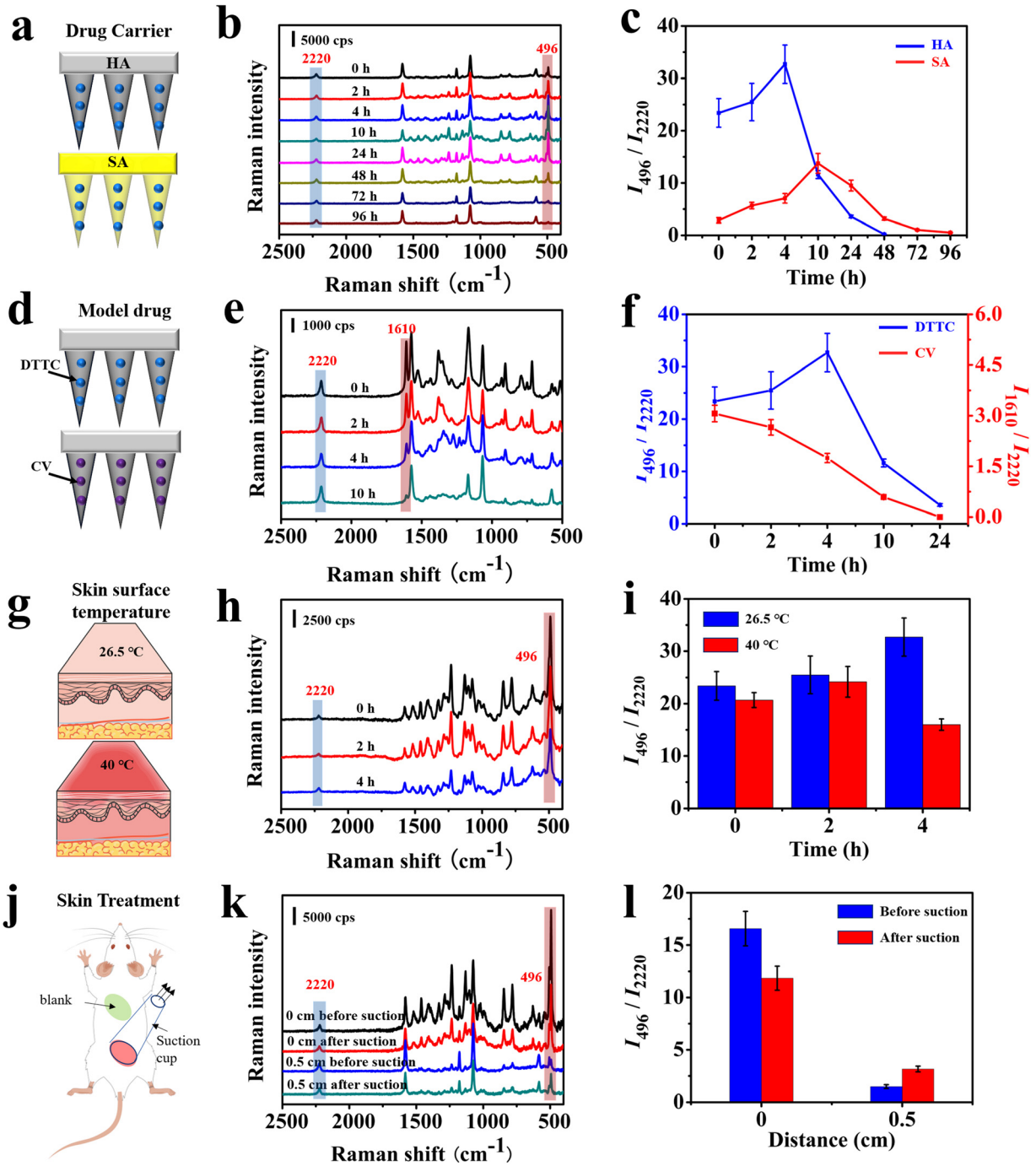

Fig. 4 Investigating the effects of different factors on the release and diffusion behavior of drugs in ISF. (a) Scheme of T-MNs prepared by using HA and SA as drug carrier materials. (b) SERS spectra of DTTC at the "0" site at different times using SA MNs. (c) Evolution of the SERS intensity ratio (I_{496}/I_{2220}) of HA and SA MNs (n = 6). (d) Scheme of T-MN loading with DTTC and CV with different amphiphilicities. (e) SERS spectra of CV at the "0" site at different times. (f) Evolution of the SERS intensity ratio (I_{496}/I_{2220}) of DTTC and CV loaded MNs (n = 6). (g) Schematic diagram of the skin state at normal (26.5 °C) and heated temperature (40 °C). (h) SERS spectra of DTTC at the release site at different times at a heated temperature (40 °C). (i) Histogram of the SERS intensity ratio (I_{496}/I_{2220}) of DTTC from the two temperature conditions at different times (n = 6). (j) Schematic diagram of suction on the drug release site. The green circle indicates normal skin and the red circle indicates skin subjected to suction and negative pressure vacuum for 3–5 seconds each time and repeated three times. (k) SERS spectra of DTTC in the drug release region before and after suction. (l) Histogram comparing the SERS intensity ratio I_{496}/I_{2220} in the drug release site before and after suction.

to achieve the advantages of controlled drug release. In this work, DTTC and CV were selected as model drugs due to their intrinsic strong SERS signals. In the future, the analytes can be extended to a variety of SERS-inactive drugs by the development of more sensitive SERS MNs (such as silver NP-based MNs) or indirect SERS sensing mechanisms.[43,44]

Materials and methods

Materials

Poly(styrene-*b*-4-vinylpyridine) (PS-*b*-P4VP, 41 kg mol^{-1} PS content and 20 kg mol^{-1} P4VP content) was synthesized by Xian Ruixi Biological Technology Co., Ltd. 4-Mercaptobenzonitrile (4-MBN) was purchased from Bide Pharmatech Co., Ltd. Chloroauric acid ($HAuCl_4$), polyvinylpyrrolidone-k30 (PVP-K30), sodium citrate, tetrahydrofuran (THF), crystal violet (CV), silver nitrate ($AgNO_3$) and L-ascorbic acid (AA) were obtained from Sinopharm Chemical Reagent Co., Ltd. 3,3′-Diethylthiatricarbocyanine (DTTC), cetyltrimethylammonium bromide (CTAB) and sodium alginate (SA, low viscosity) were obtained from Sigma-Aldrich. Hyaluronic acid (HA, 150–250 K) was purchased from Shanghai Yuanye Biological Technology Co., Ltd. Poly-(methyl methacrylate) (PMMA) MNs and poly-(dimethyl siloxane) (PDMS) molds were obtained from Taizhou Microchip Pharmaceutical Technology Co., Ltd. Deionized water was used in all the experiments.

Characterization

SERS spectra of MNs were obtained using a DXR Raman microscope (Thermo Scientific, USA) with a 780 nm laser and a 20× objective. The detection laser power was 20 mW and the exposure time was 1 s. SEM images were obtained on an S-4800 field emission scanning electron microscope (Hitachi, Japan). The CLSM image is from a Leica Sp8 confocal microscope (Leica, Germany).

Animals

All experiments were performed in accordance with the Guide for the Care and Use of Laboratory Animals of the National Institutes of Health. The experimental plan was approved by the Animal Care and Use Committee of the Binzhou Medical College, Yantai, China (Approval Number: 2022-408). KM female mice of a weight of about 25 g were used in all experiments. The mice were kept stable for 7 days under standard rearing conditions (light/dark cycle for 12 h, temperature 22 °C) before all experiments.

Preparation of therapeutic microneedles (T-MN)

DTTC solid dispersions were prepared first. Briefly, DTTC (0.0054 g) and PVP-k30 (0.043 g) were mixed and dissolved with a sufficient amount of anhydrous ethanol, followed by rotary evaporation at 40 °C and dried under vacuum at 50 °C for 12 h. The solid dispersions were obtained by crushing and passing through a 100-mesh sieve. Then, 0.01 g of DTTC solid dispersion and 0.04 g of HA were dissolved in 1 mL of deionized water at 45 °C. Subsequently, this filled a PDMS mold (10 × 10 array, 800 μm height) with 100 μL of HA-DTTC solution and the mold was kept under vacuum for 10 min, followed by drying at 45 °C for 4 h. Finally, T-MNs were obtained by careful separation from the PDMS mold.

Preparation of SERS detection microneedles (D-MNs)

SERS D-MNs were prepared according to our previous work.[28] First, 100 mL of 0.01% $HAuCl_4$ was added to a round-bottom flask and boiled under stirring reflux. Then 1 mL of 1% sodium citrate was added and boiled for 30 min to prepare nearly 40 nm of spherical AuNPs. After cooling to room temperature, the pH was adjusted to 4.74. Then the PMMA MNs were rinsed with ethanol and deionized water, and immersed in 200 μL of PS-*b*-P4VP (0.2 mg mL^{-1}) solution for 5 min, followed by rinsing with deionized water. Subsequently, the PMMA MNs were immersed in 200 μL of AuNP solution for 24 h. After rinsing with a sufficient amount of deionized water, the PMMA MNs were further immersed in 200 μL of 4-MBN (10^{-4} M) solution overnight. Finally, D-MNs were obtained by immersing the above PMMA MNs in Au^+ growth solution composed of $AgNO_3$ (114 μL, 0.01 M), CTAB (3 mL, 0.2 M), $HAuCl_4$ (192 μL, 40 mM), DI water (5.5 mL), AA (480 μL, 0.1 M) for 30 min.

Investigating the diffusion behavior of DTTC in ISF

Lateral diffusion of DTTC was investigated first. For investigation of diffusion direction, T-MNs were pressed onto the skin of the mice for 10 min to release DTTC in ISF. One D-MN was located at the release site (marked by "0") and four D-MNs were located around the "0" site (marked by "a" to "d") with an equal distance of 0.5 cm. After the D-MNs had been inserted into these five sites for 10 min, they were removed from the mouse skin and the SERS signal at the tip was measured. For diffusion distance investigation, detection sites were set at 0.5 cm intervals upward, starting at the upper border of the drug release site. Then, vertical diffusion of DTTC in ISF was studied. After T-MNs were inserted into the dorsal skin of the mice for 10 min, SERS intensities at the "0" site and 0.5 cm diffusion sites were dynamically monitored at 0, 1, 4, 10, and 24 h using fresh D-MNs at each time point. During SERS measurement, the D-MNs were lengthwise oriented on a glass slide and the sharpest region of a tip was selected for laser spot focusing and SERS detection. The signals from the 6 tips of the MNs were recorded from the two outer sides with laser power 20 mW and exposure time 1 s. The average intensity ratio of drug and IS was calculated to indicate the drug concentration in the detection area.

Investigating the effects of different factors on drug release and diffusion behavior in ISF

To investigate different drug carrier materials, DTTC-loaded SA T-MNs (ESI†) and HA T-MNs were first inserted into the mouse skin for 10 min to release the drug. Then, T-MNs were used to detect the SERS signal at the DTTC release sites after 0, 2, 4, 10, 24, 48, 72, and 96 h. To investigate different drug models, CV-loaded T-MNs (see detailed preparation procedure in ESI†) and DTTC-loaded T-MNs were inserted into the mouse skin for 10 min to release the drug. Subsequently, the SERS signals of DTTC at the release sites after 0, 2, 4, 10, and 24 h were monitored by D-MNs. To investigate the effect of skin temperature, DTTC-loaded T-MNs were inserted into the mouse skin for 10 min. Then, the skin surface temperature of the drug release site was increased to 40 °C by a heat lamp. The temperature was recorded by an NIR infrared thermal imager. The SERS signals of DTTC at the release sites after 0, 2, and 4 h were detected by D-MNs. To investigate the effect of suction, after DTTC was

released into the ISF, D-MNs were inserted at the release site (0 cm) and diffusion site (0.5 cm) for SERS detection before and after suction. For all the SERS detections, D-MNs were inserted into the drug release site for 10 min and then removed for detection.

Author contributions

L. C. and Y. W. designed the experiment. S. S., R. M. and X. Z. analyzed the data and wrote the first draft. All authors contributed extensively to the conduction of the experiments and the revision of this paper.

Conflicts of interest

The authors declare no competing financial interests.

Acknowledgements

This study was financially supported by the National Nature Science Foundation of China (No. 42076199, 21976209), the Instrument Developing Project of the Chinese Academy of Sciences (YZ201662) and Taishan Scholar Project Special Funding (No. tsqn202211262, ts20190962).

References

1 J. Yang, J. Yang, X. Gong, Y. Zheng, S. Yi, Y. Cheng, Y. Li, B. Liu, X. Xie, C. Yi and L. Jiang, *Adv. Healthcare Mater.*, 2022, **11**, e2102547.
2 H. Chang, S. W. T. Chew, M. Zheng, D. C. S. Lio, C. Wiraja, Y. Mei, X. Ning, M. Cui, A. Than, P. Shi, D. Wang, K. Pu, P. Chen, H. Liu and C. Xu, *Nat. Biomed. Eng.*, 2021, **5**, 1008–1018.
3 Y. Huang, H. Li, T. Hu, J. Li, C. K. Yiu, J. Zhou, J. Li, X. Huang, K. Yao, X. Qiu, Y. Zhou, D. Li, B. Zhang, R. Shi, Y. Liu, T. H. Wong, M. Wu, H. Jia, Z. Gao, Z. Zhang, J. He, M. Zheng, E. Song, L. Wang, C. Xu and X. Yu, *Nano Lett.*, 2022, **22**, 5944–5953.
4 Y. Li, G. He, L. H. Fu, M. R. Younis, T. He, Y. Chen, J. Lin, Z. Li and P. Huang, *ACS Nano*, 2022, **16**, 17298–17312.
5 M. Yin, J. Wu, M. Deng, P. Wang, G. Ji, M. Wang, C. Zhou, N. T. Blum, W. Zhang, H. Shi, N. Jia, X. Wang and P. Huang, *ACS Nano*, 2021, **15**, 17842–17853.
6 D. Yang, M. Chen, Y. Sun, Y. Jin, C. Lu, X. Pan, G. Quan and C. Wu, *Acta Biomater.*, 2021, **121**, 119–133.
7 J. Li, H. Lu, Y. Wang, S. Yang, Y. Zhang, W. Wei, Y. Qiao, W. Dai, R. Ge and H. Dong, *Anal. Chem.*, 2022, **94**, 968–974.
8 Y. Wu, F. Tehrani, H. Teymourian, J. Mack, A. Shaver, M. Reynoso, J. Kavner, N. Huang, A. Furmidge, A. Duvvuri, Y. Nie, L. M. Laffel, F. J. Doyle 3rd, M. E. Patti, E. Dassau, J. Wang and N. Arroyo-Curras, *Anal. Chem.*, 2022, **94**, 8335–8345.
9 K. Y. Goud, C. Moonla, R. K. Mishra, C. Yu, R. Narayan, I. Litvan and J. Wang, *ACS Sens.*, 2019, **4**, 2196–2204.
10 R. Jamaledin, P. Makvandi, C. K. Y. Yiu, T. Agarwal, R. Vecchione, W. Sun, T. K. Maiti, F. R. Tay and P. A. Netti, *Adv. Ther.*, 2020, **3**, 2000171.
11 M. Dervisevic, M. Alba, L. Yan, M. Senel, T. R. Gengenbach, B. Prieto-Simon and N. H. Voelcker, *Adv. Funct. Mater.*, 2021, **32**, 2009850.
12 E. Laszlo, G. De Crescenzo, A. Nieto-Argüello, X. Banquy and D. Brambilla, *Adv. Funct. Mater.*, 2021, **31**, 2106061.
13 C. Kolluru, R. Gupta, Q. Jiang, M. Williams, H. Gholami Derami, S. Cao, R. K. Noel, S. Singamaneni and M. R. Prausnitz, *ACS Sens.*, 2019, **4**, 1569–1576.
14 Y. Xue, C. Chen, R. Tan, J. Zhang, Q. Fang, R. Jin, X. Mi, D. Sun, Y. Xue, Y. Wang, R. Xiong, H. Lu and W. Tan, *ACS Appl. Mater. Interfaces*, 2022, **14**, 37396–37409.
15 J. Plou, B. Molina-Martinez, C. Garcia-Astrain, J. Langer, I. Garcia, A. Ercilla, G. Perumal, A. Carracedo and L. M. Liz-Marzan, *Nano Lett.*, 2021, **21**, 8785–8793.
16 K. Ahmed Saeed Al-Japairai, S. Mahmood, S. Hamed Almurisi, J. Reddy Venugopal, A. Rebhi Hilles, M. Azmana and S. Raman, *Int. J. Pharm.*, 2020, **587**, 119673.
17 K. Jiang, D. Zhao, R. Ye, X. Liu, C. Gao, Y. Guo, C. Zhang, J. Zeng, S. Wang and J. Song, *Nanoscale*, 2022, **14**, 1834–1846.
18 C. Herkenne, I. Alberti, A. Naik, Y. N. Kalia, F. X. Mathy, V. Preat and R. H. Guy, *Pharm. Res.*, 2008, **25**, 87–103.
19 L. van Smeden, A. Saris, K. Sergelen, A. M. de Jong, J. Yan and M. W. J. Prins, *ACS Sens.*, 2022, **7**, 3041–3048.
20 R. K. Mishra, K. Y. Goud, Z. Li, C. Moonla, M. A. Mohamed, F. Tehrani, H. Teymourian and J. Wang, *J. Am. Chem. Soc.*, 2020, **142**, 5991–5995.
21 Y. Cheng, X. Gong, J. Yang, G. Zheng, Y. Zheng, Y. Li, Y. Xu, G. Nie, X. Xie, M. Chen, C. Yi and L. Jiang, *Biosens. Bioelectron.*, 2022, **203**, 114026.
22 Y. Zeng, J. Wang, Z. Wang, G. Chen, J. Yu, S. Li, Q. Li, H. Li, D. Wen, Z. Gu and Z. Gu, *Nano Today*, 2020, **35**, 100984.
23 J. Zhu, X. Zhou, H. J. Kim, M. Qu, X. Jiang, K. Lee, L. Ren, Q. Wu, C. Wang, X. Zhu, P. Tebon, S. Zhang, J. Lee, N. Ashammakhi, S. Ahadian, M. R. Dokmeci, Z. Gu, W. Sun and A. Khademhosseini, *Small*, 2020, **16**, e1905910.
24 H. Teymourian, C. Moonla, F. Tehrani, E. Vargas, R. Aghavali, A. Barfidokht, T. Tangkuaram, P. P. Mercier, E. Dassau and J. Wang, *Anal. Chem.*, 2020, **92**, 2291–2300.
25 Y. Wang, C. Zhao, J. Wang, X. Luo, L. Xie, S. Zhan, J. Kim, X. Wang, X. Liu and Y. Ying, *Sci. Adv.*, 2021, **7**, eabe4553.
26 J. Ju, C. M. Hsieh, Y. Tian, J. Kang, R. Chia, H. Chang, Y. Bai, C. Xu, X. Wang and Q. Liu, *ACS Sens.*, 2020, **5**, 1777–1785.
27 J. E. Park, N. Yonet-Tanyeri, E. Vander Ende, A. I. Henry, B. E. Perez White, M. Mrksich and R. P. Van Duyne, *Nano Lett.*, 2019, **19**, 6862–6868.
28 R. Mei, Y. Wang, S. Shi, X. Zhao, Z. Zhang, X. Wang, D. Shen, Q. Kang and L. Chen, *Anal. Chem.*, 2022, **94**, 16069–16078.
29 Y. Yang, H. Chu, Y. Zhang, L. Xu, R. Luo, H. Zheng, T. Yin and Z. Li, *Nano Res.*, 2022, **15**, 8336–8344.
30 M. Zheng, Z. Wang, H. Chang, L. Wang, S. W. T. Chew, D. C. S. Lio, M. Cui, L. Liu, B. C. K. Tee and C. Xu, *Adv. Healthcare Mater.*, 2020, **9**, e1901683.
31 A. Yuan, F. Xia, Q. Bian, H. Wu, Y. Gu, T. Wang, R. Wang, L. Huang, Q. Huang, Y. Rao, D. Ling, F. Li and J. Gao, *ACS Nano*, 2021, **15**, 13759–13769.

32 Y. Zhang, J. Qian, D. Wang, Y. Wang and S. He, *Angew. Chem., Int. Ed.*, 2013, **52**, 1148–1151.
33 H. Li, Y. Yin, C. Yang, M. Chen, F. Wang, C. Ma, H. Li, Y. Kong, F. Ji and J. Hu, *Cell Proliferation*, 2020, **53**, e12760.
34 Y. Zhang, J. Li, M. Wu, Z. Guo, D. Tan, X. Zhou, Y. Li, S. Liu, L. Xue and Y. Lei, *ACS Appl. Bio Mater.*, 2020, **3**, 8640–8649.
35 D. Al Sulaiman, J. Y. H. Chang, N. R. Bennett, H. Topouzi, C. A. Higgins, D. J. Irvine and S. Ladame, *ACS Nano*, 2019, **13**, 9620–9628.
36 I. Torres-Teran, M. Venczel and S. Klein, *Int. J. Pharm.*, 2021, **610**, 121257.
37 S. H. Shin, M. Yu, D. C. Hammell, P. Ghosh, S. G. Raney, H. E. Hassan and A. L. Stinchcomb, *J. Controlled Release*, 2022, **342**, 134–147.
38 K. S. Kim and L. Simon, *Comput. Chem. Eng.*, 2011, **35**, 1152–1163.
39 D. G. Wood, M. B. Brown and S. A. Jones, *Int. J. Pharm.*, 2011, **404**, 42–48.
40 H. Ashigai, Y. Taniguchi, Y. Matsukura, E. Ikeshima, K. Nakashima, M. Mizutani and H. Yajima, *J. Agric. Food Chem.*, 2018, **66**, 1251–1257.
41 M. Vaccaro, M. Coppola, M. Ceccarelli, M. Montopoli and C. Guarneri, *Eur. Rev. Med. Pharmacol. Sci.*, 2021, **25**, 2327–2330.
42 E. O. Lallow, N. C. Jhumur, I. Ahmed, S. B. Kudchodkar, C. C. Roberts, M. Jeong, J. M. Melnik, S. H. Park, K. Muthumani, J. W. Shan, J. D. Zahn, D. I. Shreiber, J. P. Singer, Y. K. Park, J. N. Maslow and H. Lin, *Sci. Adv.*, 2021, **7**, eabj0611.
43 M. Arabi, A. Ostovan, Y. Wang, R. Mei, L. Fu, J. Li, X. Wang and L. Chen, *Nat. Commun.*, 2022, **13**, 5757.
44 M. Arabi, A. Ostovan, Z. Zhang, Y. Wang, R. Mei, L. Fu, X. Wang, J. Ma and L. Chen, *Biosens. Bioelectron.*, 2021, **174**, 112825.